Direct Observation of Room-Temperature Polar Ordering in Colloidal GeTe Nanocrystals

Mark J. Polking[1], Haimei Zheng[2,3], Jeffrey J. Urban[4], Delia J. Milliron[4], Emory Chan[4], Marissa A. Caldwell[5], Simone Raoux[6], Christian F. Kisielowski[2], Joel W. Ager III[7], Ramamoorthy Ramesh[1,7]*, and A. Paul Alivisatos[3,7]*

1. *Department of Materials Science and Engineering, University of California, Berkeley, Berkeley, CA 94720*

2. *National Center for Electron Microscopy, Lawrence Berkeley National Laboratory, Berkeley, CA 94720*

3. *Department of Chemistry, University of California, Berkeley, Berkeley, CA 94720*

4. *The Molecular Foundry, Lawrence Berkeley National Laboratory, Berkeley, CA 94720*

5. *Department of Chemistry, Stanford University, Stanford, CA 94305*

6. *IBM T. J. Watson Research Center, Yorktown Heights, NY 10598*

7. *Materials Sciences Division, Lawrence Berkeley National Laboratory, Berkeley CA 94720*

*Corresponding authors, email: rramesh@berkeley.edu, alivis@berkeley.edu

Abstract:

Ferroelectrics and other materials that exhibit spontaneous polar ordering have demonstrated immense promise for applications ranging from non-volatile memories to microelectromechanical systems. However, experimental evidence of polar ordering and effective synthetic strategies for accessing these materials are lacking for low-dimensional nanomaterials. Here, we demonstrate the synthesis of size-controlled nanocrystals of the polar material germanium telluride (GeTe) using colloidal chemistry and provide the first direct evidence of room-temperature polar ordering in nanocrystals less than 5 nm in size using aberration-corrected transmission electron microscopy. Synchrotron x-ray diffraction and Raman studies demonstrate a sizeable polar distortion and a reversible size-dependent polar phase transition in these nanocrystals. The stability of polar ordering in solution-processible nanomaterials suggests an economical avenue to Tbit/in^2-density non-volatile memory devices and other applications.

Ferroelectrics and related materials with a polar order parameter, or spontaneous electrical polarization, have attracted great interest for non-volatile information storage devices, high-κ dielectrics, and many other applications (*1*, *2*). Practical application of these materials, however, requires room-temperature stability of the polar phase and a detailed understanding of polar ordering at the nanoscale. The fundamental nature of polar phase stability in low-dimensional nanomaterials has remained elusive, with previous reports indicating complete quenching of the polar state below a critical length scale due to depolarization fields, surface layers, and other effects (*3*-*5*). Although recent theoretical work has predicted the emergence of stable toroidal polarization patterns and phase transitions in ferroelectric nanodots (*6*), experimental confirmation of polar phase stability and characterization of phase transitions in unconstrained low-dimensional nanosystems are noticeably lacking. This important gap has arisen partly due to the challenge of preparing crystalline, size-controlled polar nanomaterials, evinced by the scarcity of reports (*7*) relative to the abundant literature on size-controlled routes to nanoscale semiconductors and metals (*8*, *9*). Here we extend colloidal chemistry methods, which have emerged as a powerful tool for the exploration of novel size-dependent phenomena in optical, magnetic, and other functional nanomaterials (*8*, *9*), to the size-controlled colloidal synthesis of a nanomaterial with spontaneous polar ordering, the semiconductor germanium telluride (GeTe). We employ this material, the simplest known ferroelectric (*10*), as a model system for the fundamental study of the stability of the polar order parameter and polar phase transitions in nanocrystals. We provide the first direct experimental evidence of a room-temperature polar distortion in individual

4.5-8 nm nanocrystals using aberration-corrected transmission electron microscopy (TEM). Furthermore, we demonstrate the presence of a large size-dependent polar distortion and a reversible displacive phase transition in nanocrystals down to at least 5 nm in size using a combination of temperature-dependent synchrotron x-ray diffraction and Raman scattering. This work provides unambiguous experimental evidence for the existence of polar ordering and phase transitions in low-dimensional nanomaterials and suggests the feasibility of non-volatile memories with Tbit/in^2 densities.

GeTe is a IV-VI semiconductor with a band gap of approximately 0.1 eV in the bulk (*11*). At high temperatures, GeTe adopts the rock salt structure characteristic of many group IV chalcogenides (*12*, *13*). Below ~625 K, the cubic lattice undergoes a spontaneous symmetry-breaking distortion into a rhombohedral structure (space group R3m), which yields a polar phase (*12-14*). This distortion, illustrated in Fig. 1a, may be represented as an angular distortion of the unit cell with a concurrent displacement of the Ge sublattice (*15*), which generates a spontaneous polarization along any of the eight <111> axes of the original rock salt lattice. This distortion is stabilized by the symmetry-breaking hybridization of the $4s^2$ lone pair of the Ge cations with both anion and cation *p* states, which lifts the electronic degeneracy and widens the band gap (*14-16*).

The stability and size-dependence of this polar distortion were probed using several different populations of monodisperse GeTe nanocrystals synthesized by colloidal techniques. Nanocrystals with average diameters of 8 and 17 nm were prepared by reaction of the divalent germanium precursor bis[bis(trimethylsilyl)amino]Ge(II) with trioctylphosphine-tellurium, used by Tuan *et al.* for the high-pressure synthesis of GeTe

microcrystals (*17*). Nanocrystals with average diameters of 100 and 500 nm were prepared by reaction of a precursor with slower nucleation kinetics, $GeCl_2$-1,4 dioxane complex, with the same tellurium source. Full details on all syntheses may be found in the Supporting Online Material (*18*).

Typical TEM images and size statistics for all particle sizes are shown in Fig. 2. High-resolution TEM (HRTEM) imaging and powder x-ray diffraction (Fig. 3a) indicate that particles of all sizes are crystalline and composed of pure-phase GeTe with the rhombohedral symmetry characteristic of the low-temperature phase. Analysis of the 100 nm nanocrystals with electron diffraction indicates the presence of abundant {100} and {110} twin boundaries consistent with literature reports describing polarization domains in GeTe (*19*). Statistical analyses of particle size for the 8, 17, and 100 nm sizes yielded standard deviations in diameter of 10-20 percent, typical values for many colloidal synthesis procedures.

Atomically-resolved images of individual 4.5-8 nm GeTe nanocrystals provide direct evidence of the polar distortion in the smallest crystals synthesized. Measurements of the small angular distortion and sublattice displacement were completed using exit wave reconstruction of HRTEM focal series obtained with the TEAM 1 microscope, which is equipped with a spherical and chromatic aberration corrector. These reconstructions conclusively demonstrate the existence of the spontaneous angular distortion in nanocrystals down to at least ~5 nm in diameter at room temperature, as illustrated in the reconstructed phase image of one such particle viewed along the [100] zone axis in Fig. 1b. The corresponding fast Fourier transform (FFT) clearly illustrates

an angular distortion of ~1.1˚ (Fig. 3c). Analysis of reconstructed phase images also reveals the presence of the centrosymmetry-breaking sublattice displacement. A phase image of a ~5 nm nanocrystal containing a (111) twin boundary, shown in Fig. 1d, shows two distinct sections, each in a [110] zone axis orientation with {111} planes oriented perpendicular to the viewing plane. Separate germanium and tellurium columns can be clearly distinguished in the image, and the sublattice displacement, manifested in a staggering of the {111} planes perpendicular to the polarization axis, is evident in the left section of the particle. No such staggering can be observed in the right section, consistent with a polarization vector that lies in a (110) plane perpendicular to the viewing plane. The sublattice displacement (displacement of the Ge cation from the center of the unit cell) on the left side of the particle measures approximately 0.2 Å, smaller than but consistent with literature reports on the bulk displacement (~0.35 Å) (*15*). Further details of the analysis are provided in the Supporting Online Material (*18*).

To confirm the generality of this phenomenon, the existence of a polar phase transition in ensembles of nanocrystals was subsequently confirmed by temperature-dependent synchrotron powder x-ray diffraction (Fig. 3). The cubic to rhombohedral phase transition in GeTe splits each of the 111 and 220 diffraction lines (of the cubic system) into distinct 003/021 (parent 111) and 024/220 (parent 220) rhombohedral doublets. This splitting provides a clear signature of the structural phase transition. Using Rietveld refinement, trends in the lattice parameters can be quantitatively assessed (Table 1, Fig. S7). As particle size decreases, the rhombohedral angle (α) increases monotonically from 88.40 to 88.81 degrees, in close agreement with the values obtained

from the TEM analysis described above for the smallest particles. In addition, the lattice constant (a) of the smallest (8 nm) nanocrystals (5.93 Å) is significantly reduced from the value of 6.023 Å found for the largest (500 nm) particles.

Temperature ramps were executed to follow the evolution of the 202 diffraction line and of the 024/220 doublet with sample replacement between ramps to avoid sintering-related history-dependence. The 202 (rhombohedral) line remains a singlet throughout the transition and may thus be used to monitor nanocrystallite size (Fig. S6). For all particle sizes, the peak position was found to move smoothly to smaller diffraction angle over the entire temperature range (Figs. 3c, S5). The slope, which reflects the coefficient of thermal expansion, is approximately independent of size. In addition, no discontinuity is evident near the expected phase transition temperature (~625 K), consistent with previous reports (*13*, *20*) that the transition is accompanied by, at most, a very small volume change. Analysis of the size-dependence of the phase transition is only considered for the 17, 100, and 500 nm particles for which little sintering occurs during the measurement (see Supporting Online Material).

To investigate the size-dependence of the rhombohedral to cubic transition, the positions of the 024 and 220 diffraction peaks were followed as a function of temperature (Figs. 3b, 3d). Peak widths were held constant while peak positions were fit at each temperature. At room temperature, all nanocrystals exhibit rhombohedral peak splitting that decreases in magnitude for smaller particles, reflecting a reduced angular distortion. Upon heating the splitting decreases monotonically for all sizes, indicating the further reduction in distortion as the nanocrystals approach the cubic phase. For the 100 and 500

nm particles, the splitting collapses gradually at lower temperatures, then more rapidly near the expected phase transition temperature (~625 K). At higher temperatures, the doublet peaks can no longer be resolved, reflecting the structural transformation to the cubic phase. In contrast, for the 17 nm particles the doublet collapses more smoothly over the entire temperature ramp, with increasing rapidity starting as low as 425 K. Upon cooling, the doublets reappear, indicating recovery of the rhombohedral phase.

Further evidence of the displacive character of the phase transition was obtained through temperature-dependent Raman studies. Many materials with a displacive polar phase transition possess a "soft" zone-center optical phonon that decreases rapidly in energy as the phase transition temperature is approached (*21*). Group theoretical analysis of GeTe indicates that the polar distortion splits a single triply degenerate Raman-inactive F_{1u} symmetry optical mode in the cubic structure into an A_1 symmetry transverse optical mode (~125 cm^{-1} at 300 K) and a doubly degenerate E symmetry transverse optical/longitudinal optical mode (~90 cm^{-1} at 300 K), both of which are Raman-active (*22*). The former (A_1) mode was determined to be the "soft" mode, and concurrent softening of the E symmetry mode was observed with increasing temperature. Since no Raman-active modes exist in the cubic-symmetry undistorted structure, the disappearance of these modes with increasing temperature, in addition to a pronounced decline in mode energies, provides a spectroscopic signature of the phase transition.

Raman analyses of films of GeTe nanocrystals (Figs. 4, S1, S2) provide spectroscopic evidence of mode softening characteristic of a displacive phase transition. The two most prominent peaks near 85 and 130 cm^{-1} in the spectra are assigned primarily

to the two optical phonon modes of crystalline GeTe. Additional peaks of lower intensity around 165 and 230 cm^{-1} were observed in the spectra of the 8, 17, and 100 nm nanocrystals. We assign the additional modes to a contribution from a low-coordination surface layer (see Supporting Online Material).

Raman characterization of a reference sample of amorphous GeTe nanoparticles (Fig. S3) revealed four peaks around 85, 125, 165 and 230 cm^{-1}, similar to the peak positions observed in the spectra of the 8, 17, and 100 nm particles and in the spectra of amorphous GeTe thin films (*23*, *24*). However, the band around 85 cm^{-1} is far more prominent for the crystalline samples, and the bands at 165 and 230 cm^{-1} become relatively weaker at progressively larger crystal sizes. The spectra of the nanocrystals can thus be understood as containing overlapping contributions from the crystalline interiors and low-coordination surfaces. The temperature dependencies of the positions and intensities of the 85 and 130 cm^{-1} features support this interpretation. While these peaks shift only a few wavenumbers (cm^{-1}) between 82 K and 373 K for amorphous GeTe (*24*), in GeTe crystals their rapidly vanishing intensities and energy shifts of tens of wavenumbers provide a clear signature of the displacive phase transition (*22*). For 100 nm and 500 nm nanocrystals, for which the surface contribution is minimized, a rapid decline in the peak energies and the scattering intensities of the 85 and 130 cm^{-1} bands occurs with increasing temperature, indicative of the approaching phase transition. For the 8 and 17 nm nanocrystals, the 85 cm^{-1} band softens continuously from 87 K through 400 K; however, the position of the 130 cm^{-1} band is stable above ~350 K. This is ascribed to a rapid decline in scattering intensity of the crystalline A_1 phonon

approaching the phase transition, so that the weakly temperature-dependent contribution from the surface dominates at higher temperatures.

The size effects observed throughout all experiments may be rationalized with a simple model based upon heightened surface-induced internal pressure. Several reports on nanosized perovskites implicate such internal strains in explaining reductions in the observed structural distortions and transition temperatures (*5*, *25-27*). A spherical particle of radius *r* with surface energy γ experiences an internal stress given by $p = 2\gamma/r$ that may be on the order of 10^8-10^{10} Pa for common values of surface energy (*25*). Internal strains arising from free surfaces have been found to induce a phase transition from a tetragonal phase to a disordered cubic phase in isolated $BaTiO_3$ nanoparticles (*26*) and to suppress ferroelectric ordering in $BaTiO_3$ wires (*27*). Phenomenological modeling using Landau-Ginzburg-Devonshire theory by Morozovska, *et al.* further indicates sizeable shifts in bulk transition temperatures and suppression of ferroelectric ordering in spherical particles due to such surface stresses for positive values of the surface energy coefficient (i.e. compressive stress) (*25*). This result is consistent with our diffraction results, which indicate both a lattice contraction for the smallest particles and a monotonic decrease in the angular distortion as a function of particle size. Literature reports describe similar trends in GeTe under hydrostatic pressures of between 0-10 GPa (*20*, *28*, *29*), and transition pressures as low as 3.5 GPa have been reported for GeTe compressed in a solid medium (*28*). Using the bulk modulus of GeTe reported in the literature (K = 49.9 GPa) as a guideline, we estimate an effective pressure of ~2.7 GPa for the 8 nm particles (*20*). These observations are also consistent with the Raman

results, which indicate a ~25 % reduction in the energy splitting of the E and A_1 symmetry peaks at low temperatures. The convergence of these peaks towards the triply degenerate F_{1u} mode of the cubic phase provides further evidence of the partial suppression of the polar distortion in the smallest particles. The temperature-dependence of the structural parameters is also consistent with this interpretation. Due to the reduced room-temperature structural distortions, it is anticipated that the temperature required to transform nanocrystals to the cubic phase would be reduced relative to bulk material. These trends are clearly manifest in the temperature-dependence of the 024/220 doublet peak positions. While the gradual nature of the change in angular distortion and the broadened peaks prevent an unambiguous identification of the size-scaling law governing the transition temperature, the collapse of the doublet at lower temperatures for smaller particles supports this interpretation.

In summary, we have developed a facile solution-phase synthesis for size-controlled nanocrystals of the polar semiconductor GeTe and demonstrated the room-temperature stability of spontaneous polar ordering in particles down to at least 5 nm in size. Using this model system of the simplest possible ferroelectric—comprising one cation and one anion per primitive unit cell—we have probed experimentally the stability of polar ordering in unconstrained nanocrystals at the smallest sizes yet reported. X-ray diffraction and Raman spectroscopy studies clearly demonstrate a reversible structural phase transition leading to a size-dependent polar distortion, which has been directly confirmed with aberration-corrected transmission electron microscopy. This study reveals the surprising stability of polar distortions in freestanding nanometer-sized

crystals and provides a convenient platform for developing future fundamental studies of the nature of polar ordering at atomic length scales.

References:

1. J. F. Scott, C. A. Paz de Araujo, *Science* **246**, 1400-1405 (1989).

2. J. F. Scott, *Science* **315**, 954-959 (2007).

3. S. Chattopadhyay, P. Ayyub, V. R. Palkar, M. Multani, *Phys. Rev. B* **52**, 13177-13183 (1995).

4. W. L. Zhong, Y. G. Wang, P. L. Zhang, B. D. Qu, *Phys. Rev. B* **50**, 698-703 (1994).

5. K. Uchino, E. Sadanaga, T. Hirose, *J. Amer. Ceram. Soc.* **72**, 1555-1558 (1989).

6. I. I. Naumov, L. Bellaiche, H. Fu, *Nature* **432**, 737-740 (2004).

7. S. O'Brien, L. Brus, C. B. Murray, *J. Am. Chem Soc.* **123**, 12085-12086 (2001).

8. C. B. Murray, *et al.*, *IBM J. Res. Dev.* **45**, 47-56 (2001).

9. J. Park, J. Joo, S. G. Kwon, Y. Jang, T. Hyeon, *Angew. Chem. Int. Ed.* **46**, 4630-4660 (2007).

10. M. E. Lines, A. M. Glass, *Principles and Applications of Ferroelectrics and Related Materials* (Clarendon Press, Oxford, 1977).

11. S. K. Bahl, K. L. Chopra, *J. Appl. Phys.* **41**, 2196-2212 (1970).

12. J. Goldak, C. S. Barrett, D. Innes, W. Youdelis, *J. Chem. Phys.* **44**, 3323-3325 (1966).

13. T. Chattopadhyay, J. X. Boucherle, H. G. von Schnering, *J. Phys. C* **20**, 1431-1440 (1987).

14. N. A. Spaldin, in *Physics of Ferroelectrics: A Modern Perspective*, K. Rabe, C. H. Ahn, J.-M. Triscone, Eds. (Springer, Berlin, 2007), pp. 179-181.

15. D. Lencer, *et al.*, *Nature Mater.* **7**, 972-977 (2008).

16. U. V. Waghmare, N. A. Spaldin, H. C. Kandpal, R. Seshadri, *Phys. Rev. B* **67**, 125111 (2003).

17. H.-Y. Tuan, B. A. Korgel, *Cryst. Growth Des.* **8**, 2555-2561 (2008).

18. Materials and methods, along with supplementary discussion and data, are provided in the Supporting Online Material available on *Science* Online. References to supporting figures are denoted by "Fig. S*x*" in the text.

19. M. Snykers, P. Delavignette, S. Amelinckx, *Mater. Res. Bull.* **7**, 831-839 (1972).

20. A. Onodera, I. Sakamoto, Y. Fujii, N. Mori, S. Sugai, *Phys. Rev. B* **56**, 7935-7941 (1997).

21. J. F. Scott, *Rev. Mod. Phys.* **46**, 83-128 (1974).

22. E. F. Steigmeier, G. Harbeke, *Solid State Commun.* **8**, 1275-1279 (1970).

23. M. A. Caldwell, S. Raoux, R. Y. Wang, H.-S. Philip Wong, D. J. Milliron, *J. Mater. Chem.* (in press, DOI: 10.1039/b917024c).

24. K. S. Andrikopoulos, *et al.*, *J. Phys. Cond. Matter* **18**, 965-979 (2006).

25. A. N. Morozovska, M. D. Glinchuk, E. A. Eliseev, *Phys. Rev. B* **76**, 014102 (2007).

26. Y. Shiratori, C. Pithan, J. Dornseiffer, R. Waser, *J. Raman Spectrosc.* **38**, 1288-1299 (2007).

27. G. Geneste, E. Bousquet, J. Junquera, P. Ghosez, *Appl. Phys. Lett.* **88**, 112906 (2006).

28. S. S. Kabalkina, L. F. Vereshchagin, N. R. Serebryanaya, *Sov. Phys. JETP* **24**, 917-919 (1967).

29. A. Ciucivara, B. R. Sahu, L. Kleinman, *Phys. Rev. B* **73**, 214105 (2006).

30. The authors gratefully acknowledge Jonathan S. Owen and Dmitri V. Talapin for fruitful discussions and Bin Jiang for technical assistance. A portion of this work (synchrotron x-ray diffraction studies) was carried out at the National Synchrotron Light Source, Brookhaven National Laboratory, which is supported by the U. S. Department of Energy, Division of Materials Sciences and Division of Chemical Sciences, under contract no. DE-AC02-98CH10886. TEM studies were performed at the National Center for Electron Microscopy, Lawrence Berkeley National Laboratory, which is supported by the Office of Science, Office of Basic Energy Sciences, of the U. S. Department of Energy under contract no. DE-AC02-05CH11231. A portion of this work (analysis of synchrotron x-ray data) was completed at the Molecular Foundry, Lawrence Berkeley National Laboratory, which is supported by the Office of Science, Office of Basic Energy Sciences, of the U. S. Department of Energy under contract no. DE-AC02-05CH11231. All other work was supported by the Director, Office of Science, Office of Basic Energy Sciences, Materials Sciences and Engineering Division, of the U. S. Department of Energy under contract no. DE-AC02-05CH11231.

Table 1. Structural parameters for GeTe nanocrystals obtained by Rietveld refinement of room-temperature synchrotron x-ray diffraction patterns. A substantial reduction in the lattice constant is evident for the smallest nanocrystals. In addition, a monotonic increase in the rhombohedral angle is observed.

Size (nm)	a (Å)	α (degrees)
8	5.93±0.03	88.81±0.02
17	5.96±0.01	88.72±0.01
100	6.017±0.005	88.599±0.004
500	6.023±0.005	88.395±0.005

Supporting Online Material:

www.sciencemag.org

Materials and Methods

Figs. S1-S7

Supporting Online Text

Figure Captions:

Fig. 1. Spontaneous polar distortion in GeTe nanocrystals. **(A)** Primitive unit cells for the cubic phase of GeTe, stable above ~625 K, and the low-temperature rhombohedral phase. The distortion results in a relative displacement of the Ge and Te sublattices that induces a spontaneous polarization (large red arrow) along a [111] axis. The displacement of the Ge cation is exaggerated for clarity. (Structural parameters obtained from ref. 15.) **(B)** Phase of the reconstructed electron exit wave for a single ~4.5 nm GeTe nanocrystal in a [100] zone axis orientation. **(C)** Corresponding fast Fourier transform demonstrating an angular distortion of ~1.1˚. **(D)** Phase of the reconstructed electron exit wave of a single ~5 nm GeTe nanocrystal with a (111) twin boundary. **(E)** Corresponding line traces from the left (top) and right (bottom) sides. Separate Ge (smaller peaks) and Te (larger peaks) columns can be observed. The alternation of {111} plane spacings arising from the Ge sublattice displacement is clearly apparent in the left section of the particle. No such staggering can be observed on the right side of the particle, consistent with a polarization vector in a (110) plane perpendicular to the viewing plane.

Fig. 2. Transmission electron microscopy images and size statistics for GeTe nanocrystals. **(A, D, G, J)** Low-resolution TEM images of 8 nm (A), 17 nm (D), 100 nm (G), and 500 nm (J) average diameter colloidal GeTe nanocrystals. **(B, E, H)** Typical HRTEM images of 8 nm (B), 17 nm (E), and 100 nm (H) average diameter nanocrystals.

HRTEM images indicate that all particles are crystalline. **(K)** Electron diffraction pattern for a 500 nm GeTe nanocrystal. **(C, F, I, L)** Size statistics histograms for 8 nm (C), 17 nm (F), 100 nm (I), and 500 nm (L) nanocrystals. The size distributions for 8, 17, and 100 nm particles are between 10 and 20 percent (standard deviation), while the size distribution for the 500 nm material is around 30 percent. *N* is the number of particles measured.

Fig. 3. Temperature-dependent synchrotron x-ray diffraction studies of the polar phase transition in GeTe nanocrystals. **(A)** Room-temperature synchrotron powder x-ray diffraction patterns of GeTe nanocrystals. **(B)** Plots of diffracted intensity versus 2-theta diffraction angle and temperature for the 024/220 doublet. Convergence of the doublet peaks into a single peak of higher intensity characteristic of the cubic phase can be seen with increasing temperature. **(C)** Position of the 202 (rhombohedral) diffraction peak as a function of temperature. **(D)** Peak positions of the 024/220 (rhombohedral) doublet peaks as a function of temperature. The room-temperature peak splitting decreases for smaller particle sizes, and the doublet collapses as the rhombohedral to cubic phase transition is approached.

Fig. 4. Temperature-dependent Raman scattering studies of GeTe nanocrystals. **(A)** Typical Raman spectra for films of 8 nm, 17 nm, 100 nm, and 500 nm average diameter GeTe nanocrystals at ~87 K. All spectra contain strong peaks that can be assigned primarily to the A_1 and E symmetry optical phonon modes of crystalline GeTe. **(B)** Plot

of the energies (in cm^{-1} units) of these two most prominent bands (primarily arising from the optical phonon modes of crystalline GeTe) as a function of temperature. Clear softening of both bands is observed for all particle sizes. In addition, a considerable decrease in the low-temperature splitting of the two bands is observed with decreasing particle size.

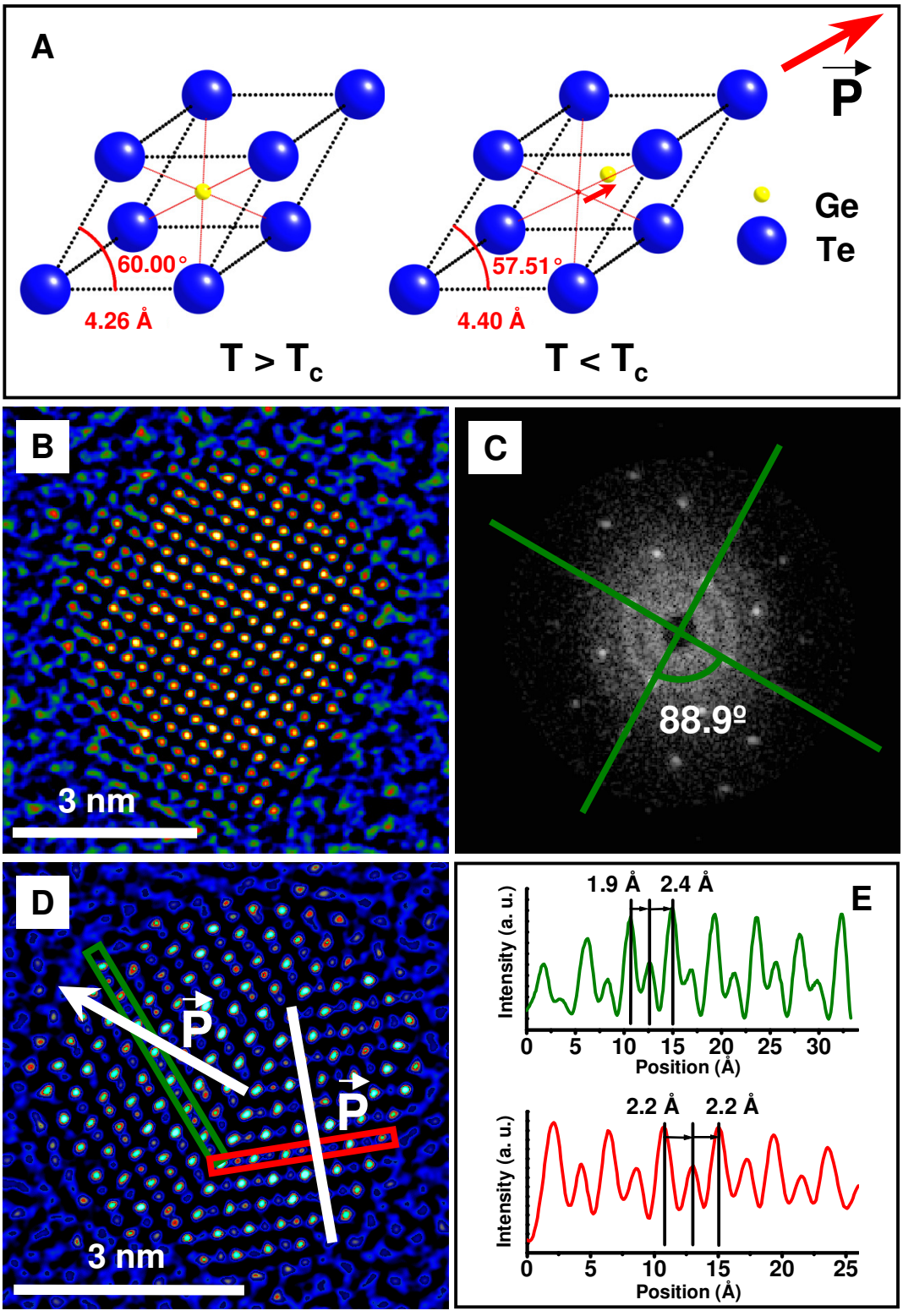
A
P
Ge
Te
60.00°
4.26 Å
T > T_c
57.51°
4.40 Å
T < T_c
B
3 nm
C
88.9º
D
P
P
3 nm
E
1.9 Å
2.4 Å
Intensity (a. u.)
0
5
10
15
20
25
30
Position (Å)
2.2 Å
2.2 Å
Intensity (a. u.)
0
5
10
15
20
25
Position (Å)

Fig. 1

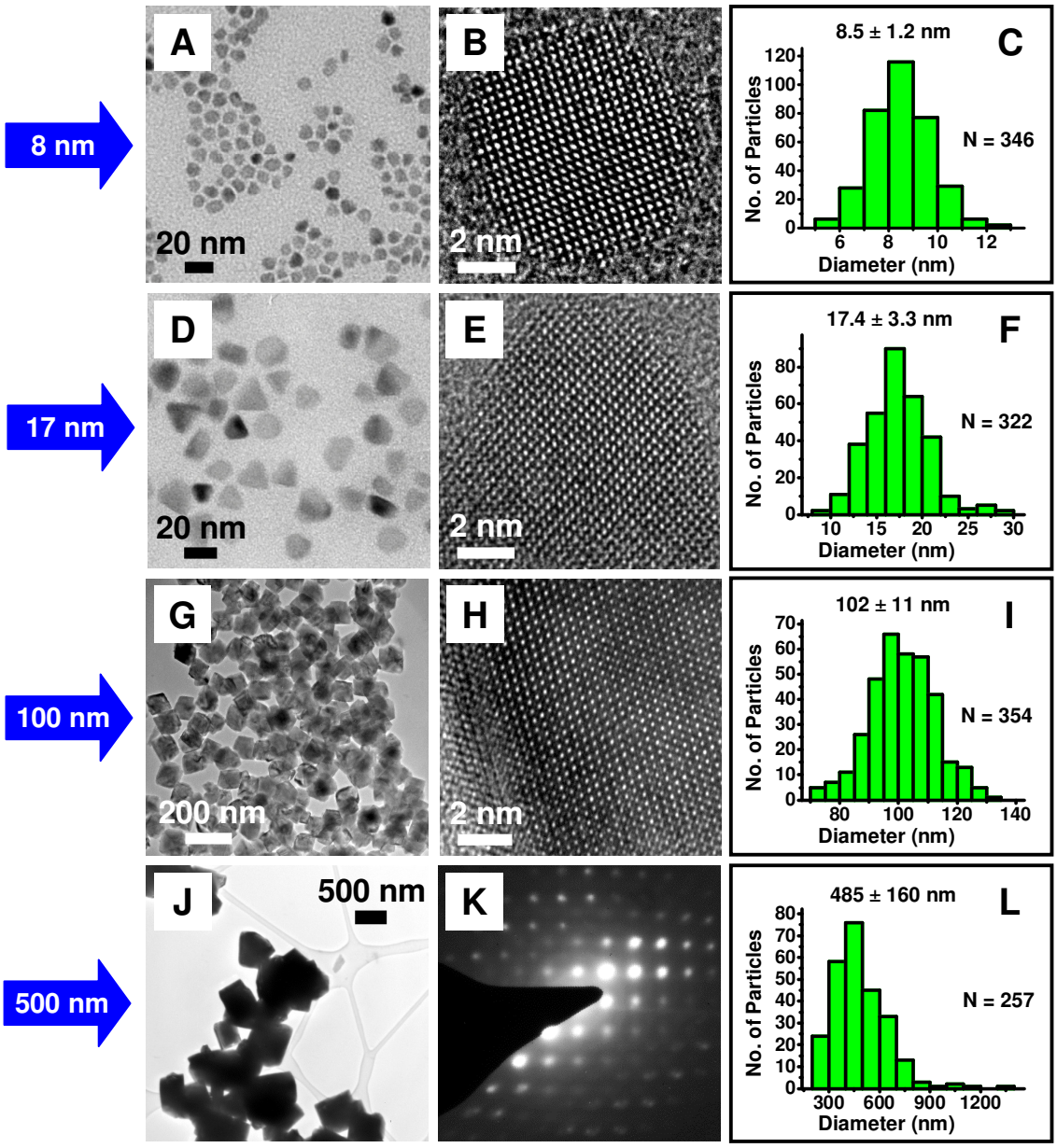
8 nm
17 nm
100 nm
500 nm
A
20 nm
B
2 nm
C
8.5 ± 1.2 nm
N = 346
No. of Particles
Diameter (nm)
D
20 nm
E
2 nm
F
17.4 ± 3.3 nm
N = 322
No. of Particles
Diameter (nm)
G
200 nm
H
2 nm
I
102 ± 11 nm
N = 354
No. of Particles
Diameter (nm)
J
500 nm
K
L
485 ± 160 nm
N = 257
No. of Particles
Diameter (nm)

Fig. 2

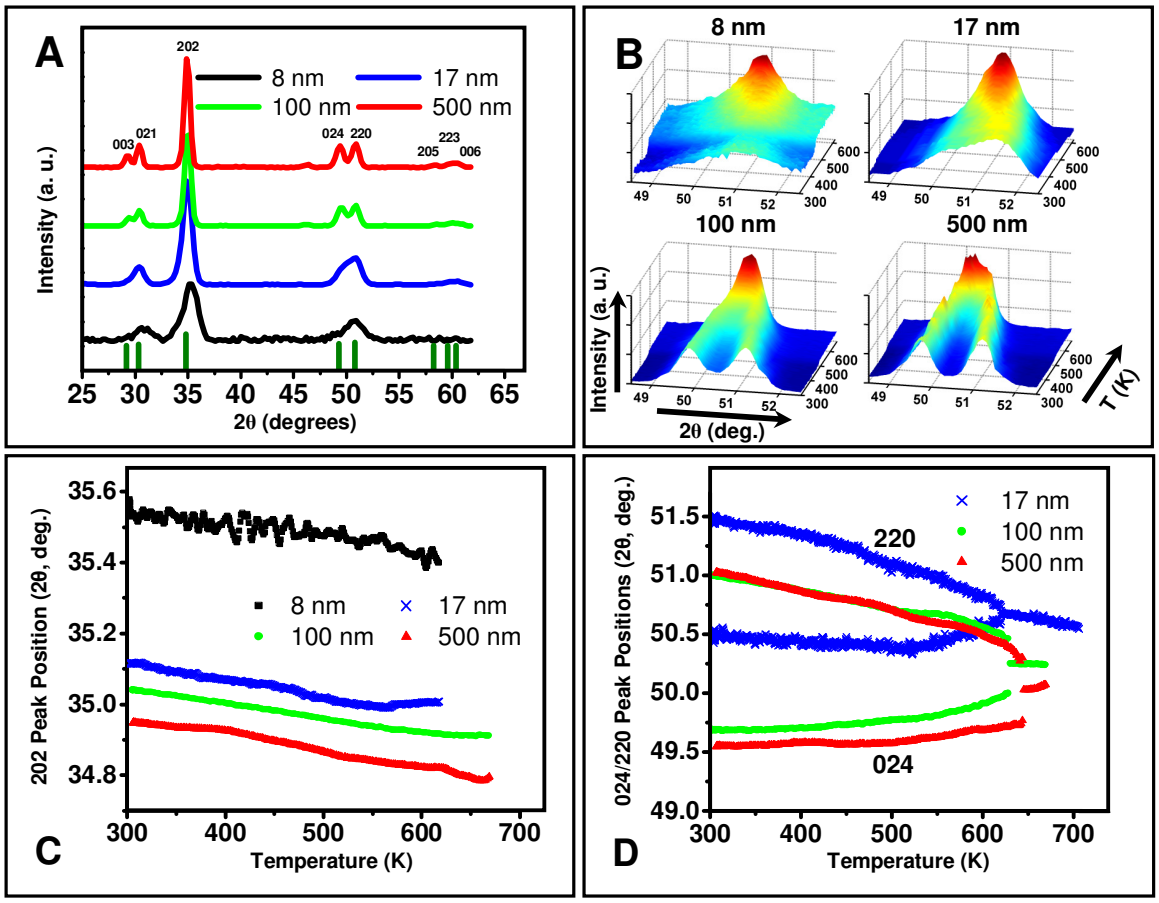
A
202
8 nm
17 nm
100 nm
500 nm
003
021
024
220
223
205
006
Intensity (a. u.)
25 30 35 40 45 50 55 60 65
2θ (degrees)
B
8 nm
17 nm
100 nm
500 nm
Intensity (a. u.)
2θ (deg.)
T (K)
C
202 Peak Position (2θ, deg.)
35.6
35.4
35.2
35.0
34.8
8 nm
17 nm
100 nm
500 nm
300 400 500 600 700
Temperature (K)
D
024/220 Peak Positions (2θ, deg.)
51.5
51.0
50.5
50.0
49.5
49.0
17 nm
100 nm
500 nm
220
024
300 400 500 600 700
Temperature (K)

Fig. 3

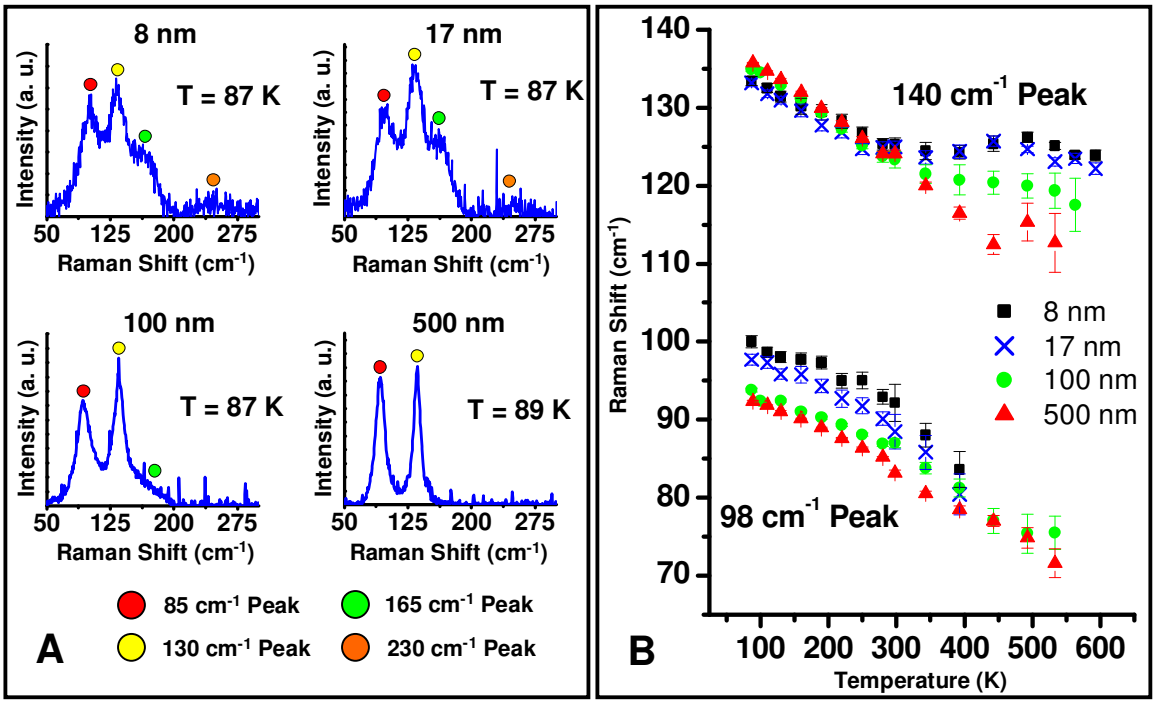
8 nm
T = 87 K
17 nm
T = 87 K
100 nm
T = 87 K
500 nm
T = 89 K
Intensity (a. u.)
Raman Shift (cm-1)
50 125 200 275
85 cm-1 Peak
165 cm-1 Peak
130 cm-1 Peak
230 cm-1 Peak
A
140 cm-1 Peak
98 cm-1 Peak
8 nm
17 nm
100 nm
500 nm
Raman Shift (cm-1)
140 130 120 110 100 90 80 70
100 200 300 400 500 600
Temperature (K)
B

Fig. 4

Supporting Online Material for "Direct Observation of Room-Temperature Polar Ordering in Colloidal GeTe Nanocrystals"

Mark J. Polking[1], Haimei Zheng[2,3], Jeffrey J. Urban[4], Delia J. Milliron[4], Emory Chan[4], Marissa A. Caldwell[5], Simone Raoux[6], Christian F. Kisielowski[2], Joel W. Ager III[7], Ramamoorthy Ramesh[1,7]*, and A. Paul Alivisatos[3,7]*

1. Department of Materials Science and Engineering, University of California at Berkeley, Berkeley, CA 94720

2. National Center for Electron Microscopy, Lawrence Berkeley National Laboratory, Berkeley, CA 94720

3. Department of Chemistry, University of California at Berkeley, Berkeley, CA 94720

4. The Molecular Foundry, Lawrence Berkeley National Laboratory, Berkeley, CA 94720

5. Department of Chemistry, Stanford University, Stanford, CA 94305

6. IBM T. J. Watson Research Center, Yorktown Heights, NY 10598

7. Materials Sciences Division, Lawrence Berkeley National Laboratory, Berkeley, CA 94720

*Corresponding authors, email: rramesh@berkeley.edu, alivis@berkeley.edu

This file includes:

Materials and Methods
Figs. S1-S7
Supporting Online Text

Reagents and Reagent Preparation:

Germanium(II) chloride-1,4 dioxane complex (1:1), tellurium powder (30 mesh, 99.997 %), 1-dodecanethiol (1-DDT, > 98 %), anhydrous 1,2 dichlorobenzene (99 %), 1-octadecene (90 %), oleylamine (70 %), oleic acid (90 %), squalane (99 %), anhydrous acetonitrile (99.8 %), and anhydrous chloroform (99 %, amylene stabilized) were purchased from Sigma-Aldrich. Bis[bis(trimethylsilyl)amino]Ge(II) (TMSNGe) was purchased from Gelest, and trioctylphosphine (TOP, 97 %) was purchased from Strem. Stock solutions of Te in TOP with a concentration of 10 wt% for the 17-500 nm particles were prepared under argon on a Schlenk line by dissolving Te powder in TOP at 200 ˚C for two hours. A 10 wt% stock solution of Te (shot, 99.999% from Sigma-Aldrich) in TOP for the 8 nm particles was prepared by dissolving Te shot in TOP at room temperature. These stock solutions were then stored in an argon glovebox. Oleic acid, 1-octadecene, squalane, and oleylamine were dried under vacuum at 110 ˚C for 1 hour, and 1-dodecanethiol was dried under vacuum at 90 ˚C for 1 hour. This drying and degassing procedure is important for the synthesis of phase-pure material. All other reagents were used without further preparation.

Synthesis of 8 nm GeTe Nanocrystals:

In a typical synthesis of 8 nm nanocrystals, 6 mL of dried squalane was added to a 50 mL 3-neck reaction flask in an argon glovebox. The flask was then sealed and

attached to a Schlenk line under constant argon flow. In the glovebox, 0.1 g of TMSNGe was mixed with 1 mL of TOP and 1 mL of dried squalane and subsequently added to the flask by syringe at room temperature. Then, 0.03 g of dried 1-DDT was mixed with 1.5 mL of a 10 wt% TOP-Te solution and loaded into a syringe. The squalane/TOP solution containing the TMSNGe precursor was then heated to 230 ˚C under constant argon flow and rapid stirring, and the 1-DDT/TOP-Te solution was immediately injected through a septum. After injection, the temperature dropped to ~220 ˚C, and the temperature was held at this value for 1.5-2 minutes. The flask was then rapidly cooled with blasts of compressed air to room temperature.

Synthesis of 17 nm GeTe Nanocrystals:

In a typical synthesis of 17 nm nanocrystals, 3 mL of dried 1-octadecene and 3 mL of dried oleylamine were loaded into a 50 mL 3-neck reaction flask inside a glovebox. In the glovebox, 0.1 g of TMSNGe was mixed with 1 mL of dried 1-octadecene and 0.5 mL of TOP-Te and loaded into a syringe. The reaction flask was sealed inside the glovebox and attached to a Schlenk line under argon flow. The flask was then heated to 250 ˚C under constant argon flow and rapid stirring, and the TMSNGe/TOP-Te injection solution was then rapidly injected through a rubber septum. The reaction mixture was held at approximately 235 ˚C for 1.5 minutes and allowed to cool to room temperature.

Synthesis of 100 nm GeTe Nanocrystals:

In a typical synthesis of 100 nm nanocrystals, 1.5 mL of dried 1-DDT, 4.5 mL of anhydrous 1,2 dichlorobenzene, and 10 mg of $GeCl_2$-dioxane were loaded into a 50 mL 3-neck reaction flask inside a glovebox. The reaction flask was sealed inside the glovebox and transferred to a Schlenk line under continuous argon flow. The reaction mixture was heated to 180 ˚C under argon flow and rapid stirring, and 0.7 mL of TOP-Te was then injected into the reaction mixture through a septum. A gradual color change from orange to red to brownish-black over approximately 10 seconds followed by eventual partial precipitation of the reaction product was observed. The reaction mixture was held at approximately 177 ˚C for 2 minutes and allowed to cool to room temperature.

Synthesis of 500 nm GeTe Nanocrystals:

In a typical synthesis of 500 nm nanocrystals, 1 mL of dried oleic acid, 1 mL of dried oleylamine, 3 mL of dried 1-octadecene, and 50 mg of $GeCl_2$-dioxane were added to a 50 mL 3-neck flask inside a glovebox, and the flask was sealed and attached to a Schlenk line under argon flow as described above. The reaction mixture was then heated to 300 ˚C under constant argon flow and stirring. At 300 ˚C, 1 mL of TOP-Te was rapidly injected into the flask through a septum. An immediate color change followed by precipitation of the reaction product was observed. The mixture was held at approximately 290 ˚C for 2 minutes and allowed to cool to room temperature.

Cleaning Procedure:

After a synthesis, the contents of the reaction vessel were transferred into a vial under argon flow and subsequently moved into a glovebox. The nanocrystals were cleaned under air-free conditions in the glovebox. In a typical cleaning procedure, ~2 mL of nanocrystal solution/suspension was mixed with 10-20 mL of anhydrous chloroform and an amount of anhydrous acetonitrile sufficient to induce flocculation of the particles (not necessary for 100 and 500 nm particles). The particles were then centrifuged at approximately 5000 RPM and redispersed in anhydrous chloroform with sonication. This centrifugation and redispersal procedure was repeated, and the particles were redispersed in chloroform for preparation of samples for TEM and other techniques.

Raman Spectroscopy:

Raman spectra were obtained using a home-built Raman system with a variable-wavelength argon ion laser operated at 514.5 nm with a laser power of 100 mW. A cylindrical lens with a spot length of several millimeters was used to minimize heating of the sample by the laser. Spectra were collected using a SPEX triple spectrometer with a 2400 lines/mm diffraction grating equipped with a liquid nitrogen-cooled CCD. Low temperature (87-280 K) measurements were done in a Janis VPF-100 liquid nitrogen cryostat controlled by a Lakeshore digital temperature controller and silicon diode sensor.

High-temperature (> 280 K) measurements were taken in a home-built resistive heating cell under constant argon flow.

Batches of nanocrystals for Raman spectroscopy similar in size to those illustrated in Fig. 2 were prepared according to the synthesis procedures described above. Particles dispersed in chloroform were then deposited on silicon substrates in an argon glovebox, and the solvent was subsequently evaporated. Before measurement, samples were coated with 50-100 nm of amorphous silica using an RF sputtering system to prevent loss of tellurium at high temperatures and minimize sintering.

Raman peaks were fit against a sloping background with PeakFit version 4 by Jandel Scientific. The Gauss*Lorentz fitting routine was employed for all peak fits. For the 8, 17, and 100 nm particles, three peaks were used in the fitting procedure; for the 500 nm particles, two peaks were employed in the fit. For the spectra presented in Fig. 4, a sloping background was subtracted in PeakFit using the NParm routine.

Full series of Raman spectra from 87 K to 593 K are presented in Figs. S1 and S2. All spectra have been normalized using the standard normal variate procedure and translated on the intensity axis for easy comparison. From these spectra, it can be observed that the intensity of the E symmetry crystalline phonon mode peak—located around 85 cm^{-1}—declines relative to the intensity of the 165 cm^{-1} mode attributed to a surface layer in the spectra of the smaller particles with increasing temperature. At high temperatures, the spectra of the 8 and 17 nm particles closely match the spectra of a ~5 nm amorphous GeTe nanoparticle control sample described below (Fig. S3). The spectra of the 100 and 500 nm particles, illustrated in Fig. S2, exhibit strong signals only from

the two phonon mode peaks of crystalline GeTe, although a small shoulder near 165 cm^{-1} is visible in the spectra of the former. Beyond 593 K in the case of the 100 nm particles, and 533 K in the case of the 500 nm particles, the Raman features become nearly impossible to fit reliably.

Discussion of the Additional Raman Modes:

A sample of amorphous nanoparticles with an average diameter of around 5 nm was employed as an experimental control to confirm the assignment of the additional Raman modes. The amorphous particles were prepared according to a procedure reported by Caldwell, *et al.* (*S1*). A series of Raman spectra for these amorphous particles is provided in Fig. S3. Comparison of these spectra with those of the 8 and 17 nm particles taken at high temperatures (> 450 K), at which the intensities of the crystalline phonon mode peaks are greatly diminished, reveals striking similarities (Figs. S1 and S3). A close correspondence, except for small temperature-induced peak shifts, exists between the spectral features of the control sample and those of the 8 and 17 nm samples taken at high temperatures. These observations confirm that the observed spectra for the 8 and 17 nm particles can be understood as a convolution of the highly temperature-dependent crystalline phonon spectrum with a contribution from a small quantity of disordered or low-coordination material. As the intensities of the crystalline phonon mode peaks diminish at higher temperatures as the structural phase transition is approached, the contribution from the disordered phase dominates, leaving a spectrum

that is in close agreement with that of the control sample. The behavior of the 130 cm^{-1} band at high temperatures may be rationalized with reference to this interpretation.

While it is difficult to rule out the presence of amorphous nanoparticles entirely, extensive surveys with HRTEM imaging reveal no evidence of such particles. Furthermore, the additional modes persist in the Raman spectra of the amorphous nanoparticle control sample after a temperature ramp to 660 K to induce complete crystallization, which occurs at ~575 K for these particles according to the work of Caldwell, *et al*. The spectra of the control sample taken after the temperature ramp closely resemble the spectra of the 8 nm particles at lower temperatures. Further, the appearance of a prominent peak near 85 cm^{-1} is observed upon cooling, indicating crystallization of the material. The presence of the relatively sharp peak around 165 cm^{-1} at temperatures exceeding 590 K for the 8 and 17 nm nanocrystals indicates that the disordered phase remains stable well above the bulk crystallization temperature of 420 K and that the additional modes are unlikely to be attributable to amorphous nanoparticles of appreciable size. A previous study on the crystallization of ultrathin phase-change films revealed an elevation of the amorphous to crystalline phase transition temperature of as much as 200 K with decreasing film thickness (*S2*). In addition, Caldwell, *et al*. report an elevation of the crystallization temperature in amorphous GeTe nanoparticles to approximately 675 K for the smallest (1.8 nm) particles employed in the study (*S1*). The continued presence of the 165 and 230 cm^{-1} bands at the highest temperatures examined in this study (~590 K) (and the continued presence of these modes in the amorphous

nanoparticle control sample after a ramp to 660 K) suggests a size scale for the disordered material of less than 2 nm.

Previous Raman studies on semiconductor nanocrystals have revealed increasing spectral contributions from disordered material with decreasing particle size assigned to disordered surface layers (*S3*, *S4*). A study by Sharp *et al*. of Ge nanocrystals grown in a silica matrix revealed features characteristic of amorphous germanium in spectra of ~5 nm crystalline particles liberated from the matrix by HF etching that were absent for Ge nanoparticles of equal size embedded in the matrix (*S3*). This amorphous-like contribution to the spectra was thus assigned to an amorphous surface layer on a crystalline core. Hayashi, *et al*. similarly assigned strong Raman features in the spectra of Si, Ge, and GaP nanocrystals characteristic of disordered material to a disordered surface layer (*S4*). The considerable intensity of these modes was rationalized by invoking the enhanced vibration amplitudes of surface atoms with respect to interior atoms. This interpretation is consistent with the systematic decline in the intensity of the additional modes with increasing nanocrystal diameter observed in this study.

Transmission Electron Microscopy:

Low-resolution transmission electron microscopy (TEM) images were taken with an FEI Technai G2 Super Twin transmission electron microscope operated at 200 kV and equipped with a LaB_6 filament. High-resolution TEM images of the 8 and 17 nm particles were then taken with an FEI monochromated F20 UT Technai transmission

electron microscope with a field emission gun and Gatan Image Filter operated at 200 kV. Electron diffraction patterns and high-resolution TEM images of the 100 and 500 nm particles were taken using an FEI CM 300 transmission electron microscope operated at 300 kV and equipped with a field emission gun and Gatan Image Filter. Focal series for exit wave reconstruction were taken using the TEAM 1 microscope at the National Center for Electron Microscopy, a modified FEI Titan microscope operated at 80 kV and equipped with a high-brightness field emission gun, Gatan Image Filter, and combined spherical and chromatic aberration correction system on the imaging side. Its configuration closely resembles that of the TEAM 0.5 microscope reported in the literature (*S5*). Exit wave reconstructions were completed using focal series consisting of 20 images with the Gerchberg-Saxton algorithm in the program MacTempas X by Total Resolution. All focal series were recorded with a negative coefficient of spherical aberration of -0.02 mm and a residual chromatic aberration of 0.002-0.003 mm. Measurements of particle sizes for size statistics were performed in Image-Pro Plus 4.5 on images taken on the FEI Technai G2 Super Twin microscope.

Modeling of Crystal Structure:

To establish the directions of the polarization vectors shown in Fig. 1d, a model of the crystal structure was generated using the structural parameters provided in reference 15 (main article) with the program ChemCraft, version 1.5. The polar distortion removes the equivalence of the different [110] zone axis orientations: For orientations with the

polarization lying in the viewing plane, a staggering of the {111} planes can be observed, and for orientations with the polarization vector lying in a (110) plane perpendicular to the viewing plane, no such staggering is evident. However, a small displacement of the Ge sublattice along a <100>-type direction can be observed. The in-plane component of this displacement is parallel to the in-plane component of the polarization vector. To measure the sublattice displacement, line profiles for all rows were calculated in MacTempas X. The column positions were then extracted by fitting the peaks in these line profiles with Voigt functions in the program PeakFit version 4 by Jandel Scientific. Subsequent comparison with the aforementioned structural model enabled the assignment of the polarization vector directions shown in Fig. 1d. Structural models of both halves are presented in Fig. S4. On the right side of the particle, the direction of the out-of-plane component of the polarization vector cannot be established definitively from the image alone: The two orientations shown in Fig. S4 yield identical [110] zone axis projections.

The displacement of the Ge cation from the center of the unit cell can be readily determined in the left half of the particle from the staggering of {111} planes, which are perpendicular to the viewing plane. The Ge sublattice displacement is parallel to the trigonal axis (see Fig. 1), which lies in the viewing plane, and is perpendicular to this set of {111} planes. The magnitude of the sublattice displacement is then one half of the difference between the spacings of adjacent pairs of {111} planes.

X-ray Diffraction:

The powder diffraction file mentioned in the text (00-047-1079) was obtained from the ICDD PDF-2 database (2006 release). The rhombohedral diffraction lines mentioned in the text refer to the unit cell described in this file. Temperature-dependent x-ray diffraction measurements were conducted at beamline X20C at the National Synchrotron Light Source at Brookhaven National Laboratory. The beamline is equipped with a high-throughput synthetic multilayer monochromator and delivers 10^{13} photons/s at a wavelength of 1.797 Å. The endstation includes a BN heater stage, and samples were heated in a purified He atmosphere. The intensity of diffracted x-ray peaks was recorded over a 2-theta range of 15˚ using a fast linear diode array detector which was centered at either 2-theta = 31˚ or 51˚ for study of the 003/021 and 024/220 doublets, respectively. Heating and cooling rates were 1 K/s.

The peak positions of the 024/220 doublet were fit with a double Gaussian expression using the Multipeak Fitting package in Igor Pro 6.1. For each size, the relative area of the 024 peak with respect to the 220 peak was constrained to within ±10 %. The doublet was considered to have collapsed when the least squares fit failed to converge using the above constraint or when the chi squared values of the fits diverged. The resulting single peak was fit using a single Gaussian expression.

GeTe nanocrystals for the x-ray diffraction experiments of similar sizes to those presented in Fig. 2 were prepared according to the synthesis procedures described above. Samples for the x-ray diffraction study were prepared by spin coating a dispersion of

nanocrystals in chloroform onto a silicon substrate cleaned by plasma etching. The resulting nanocrystal films were subsequently coated with ~10 nm of amorphous SiO_2 using RF sputtering to prevent loss of tellurium at high temperatures and minimize sintering.

Raw synchrotron x-ray diffraction data for all four nanocrystal sizes studied are presented in Fig. S5. In these scans, the intensities of the 003/021 doublet peaks and the 202 singlet peak are plotted as a function of both temperature and scattering angle. The collapse of the 003/021 doublets can be observed above ~625 K.

Rietveld refinements on the room-temperature diffraction patterns were performed in the program X'Pert HighScore Plus by PANalytical Inc. A background determined by the method of Sonneveld and Visser using a granularity constant of 15 and a bending factor of zero was subtracted from the original data for presentation in Fig. 3a. Parameters refined to produce the Rietveld fits included a zero shift for 2-theta offset, a scale factor, the lattice constants and Ge atom Z position (sublattice displacement), and the Caglioti profile factor W (peak broadening). In addition, a polynomial background fit with three parameters was employed in the Rietveld refinements. A silicon standard was employed to account for instrumental broadening. The error values reported in Table 1 are those given by the fitting software.

The broadenings of the 202 singlet peak for all particle sizes as a function of temperature for both the heating and cooling stages of the experiment are presented in Fig. S6. During the temperature ramp, the width of this peak does not change significantly for the 100 nm and 500 nm nanocrystals. The peak does narrow, however,

for the 17 nm and 8 nm diameter nanocrystals beginning around 495 K and 450 K, respectively, and this narrowing does not reverse upon cooling. This result is most consistent with sintering. For the 17 nm particles the width decreases by less than 10 %, reflecting only limited crystallite growth, while for the 8 nm particles the decrease is ~40 %. Analysis of the polar phase transition was thus restricted to the 17, 100, and 500 nm nanocrystals that exhibited little sintering during the measurement.

Size-Dependence of the Polar Distortion:

A plot of the angular distortion, normalized to the bulk value of 1.65˚ reported by Bahl, *et al.*, (*S6*), as a function of particle diameter is presented in Fig. S7a. It is an assumption of the classical theory of ferroelectrics that the square of the spontaneous polarization is proportional to the magnitude of the structural distortion (*S7*). A plot of the square root of the spontaneous angular distortion as a function of particle size thus provides a rough means of comparing the trends observed with decreasing crystal size with literature reports. Such a plot is provided in Fig. S7b. While the trend in this plot is qualitatively similar to the trends predicted by Junquera, *et al.* and Mehta, *et al.* for ferroelectric thin films (*S8*, *S9*) and the trends predicted by Zhong, *et al.*, Wang, *et al.*, and other groups for ferroelectric nanoparticles (S*10*, *S11*), the number of data points is, at present, insufficient to enable a reliable fit to a phenomenological model.

Supporting References:

S1. M. A. Caldwell, S. Raoux, R. Y. Wang, H.-S. Philip Wong, D. J. Milliron, *J. Mater. Chem.* (in press, DOI: 10.1039/b917024c).

S2. S. Raoux, J. L. Jordan-Sweet, A. J. Kellock, *J. Appl. Phys.* **103**, 114310 (2008).

S3. I. D. Sharp, *et al.*, *J. Appl. Phys.* **97**, 124316 (2005).

S4. S. Hayashi, K. Yamamoto, *Superlattices and Microstruct.* **2**, 581-585 (1986).

S5. C. Kisielowski, *et al.*, *Microsc. Microanal.* **14**, 469-477 (2008).

S6. K. L. Chopra, S. K. Bahl, *J. Appl. Phys.* **40**, 4171-4178 (1969).

S7. A. F. Devonshire, *Phil. Mag.* **40**, 1040-1063 (1949).

S8. J. Junquera, P. Ghosez, *Nature* **422**, 506-509 (2003).

S9. R. R. Mehta, B. D. Silverman, J. T. Jacobs, *J. Appl. Phys.* **44**, 3379-3385 (1973)

S10. W. L. Zhong, Y. G. Wang, P. L. Zhang, B. D. Qu, *Phys. Rev. B* **50**, 698-703 (1994).

S11. C. L. Wang, S. R. P. Smith, *J. Phys. Cond. Matter* **7**, 7163-7171 (1995).

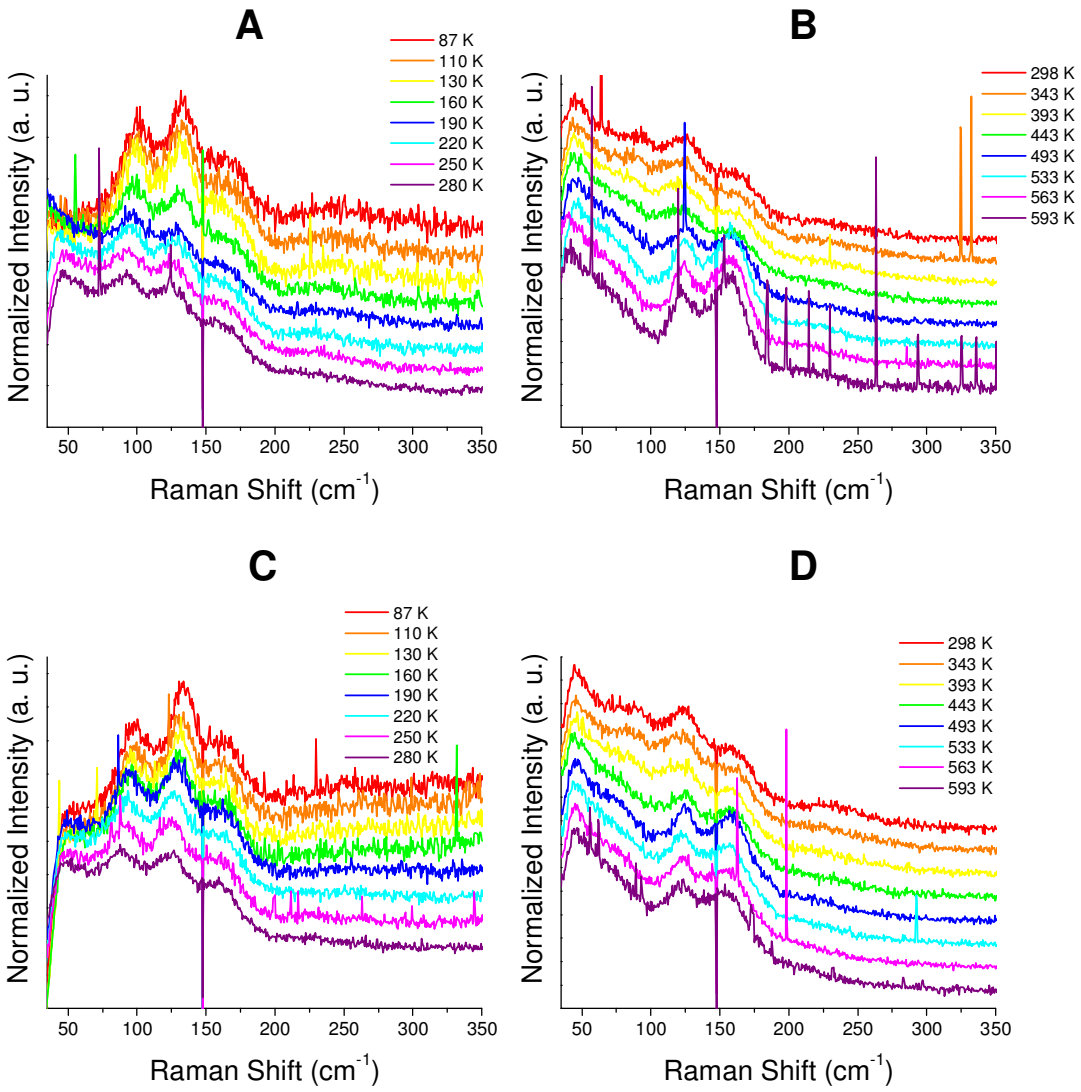

Fig. S1. Normalized Raman spectra of 8 nm and 17 nm average diameter GeTe nanocrystals from 87 K to 593 K. **(A)** Raman spectra of 8 nm particles from 87 K to 280 K. **(B)** Raman spectra of 8 nm particles from 298 K to 593 K. **(C)** Raman spectra of 17 nm particles from 87 K to 280 K. **(D)** Raman spectra of 17 nm particles from 298 K to 593 K. All spectra were normalized using the standard normal variate method and subsequently translated on the intensity axis to facilitate comparison.

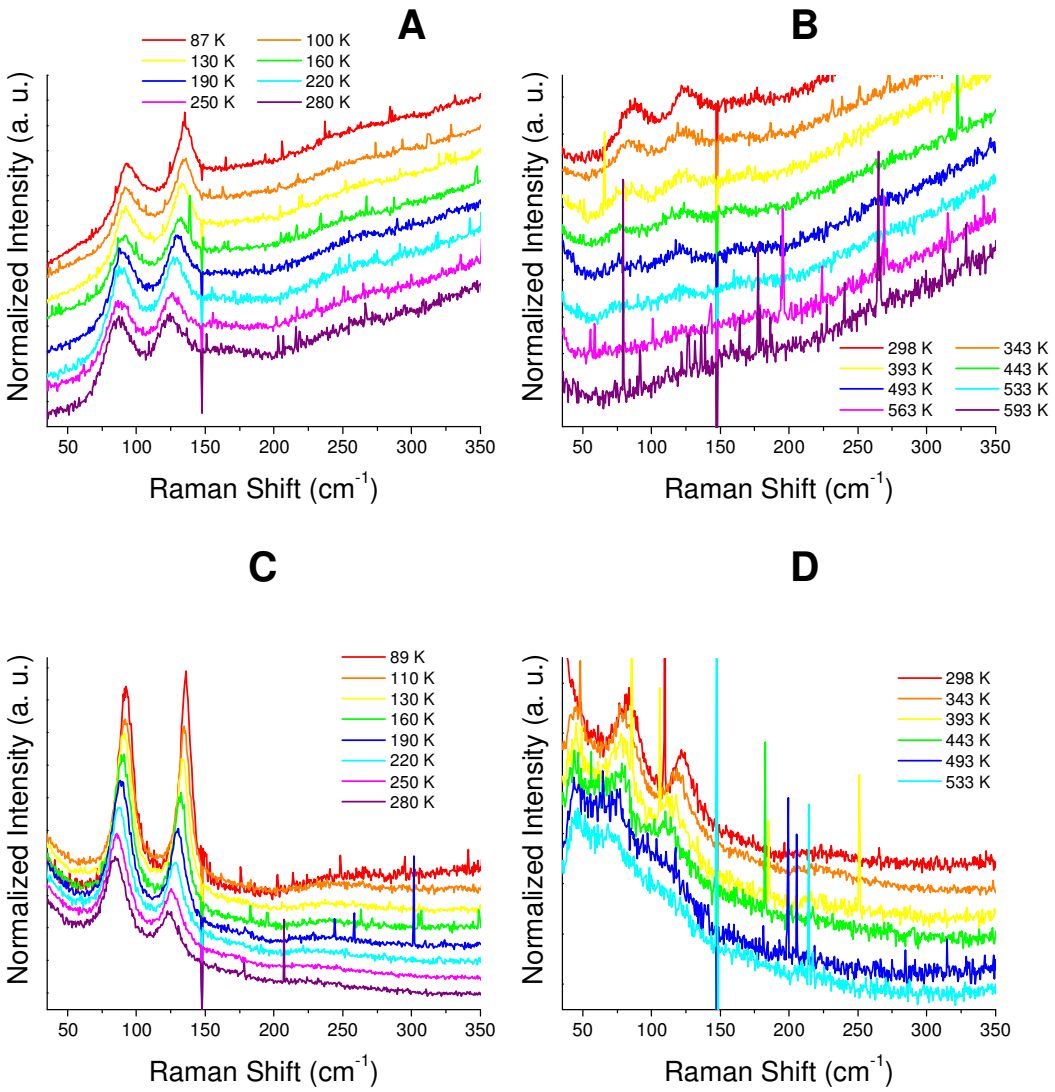

Fig. S2. Normalized Raman spectra of 100 nm and 500 nm average diameter GeTe nanocrystals from 87 K to 593 (533) K. **(A)** Raman spectra of 100 nm particles from 87 K to 280 K. **(B)** Raman spectra of 100 nm particles from 298 K to 593 K. **(C)** Raman spectra of 500 nm particles from 89 K to 280 K. **(D)** Raman spectra of 500 nm particles from 298 K to 533 K. No prominent features are evident in the Raman spectra above ~533 K. All spectra were normalized using the standard normal variate method and subsequently translated on the intensity axis to facilitate comparison.

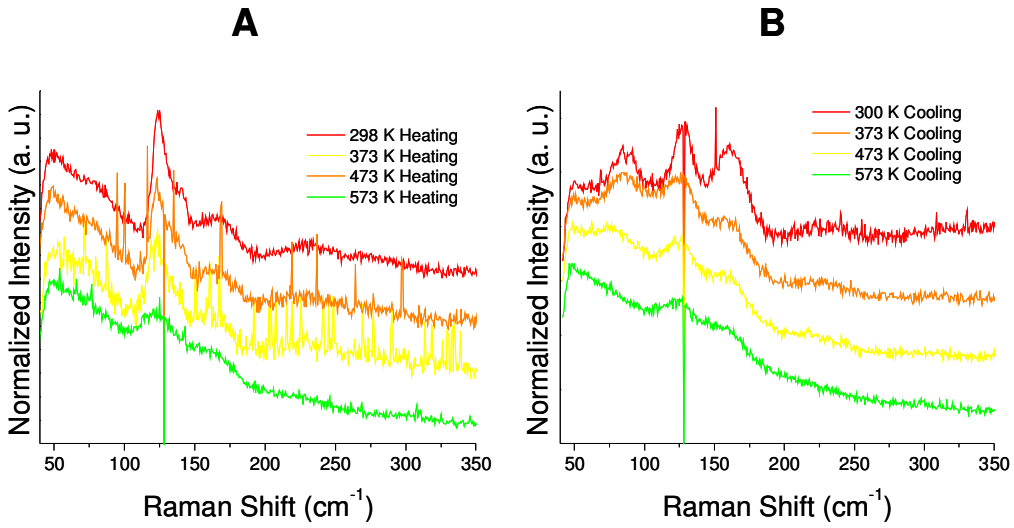

Fig. S3. Raman spectra of a control sample of ~5 nm amorphous GeTe nanoparticles during a temperature ramp to 660 K. **(A)** Raman spectra taken during the heating stage of the temperature ramp. **(B)** Raman spectra taken during the cooling stage following the ramp to 660 K. The particles crystallized during the temperature ramp, leading to the appearance of the E symmetry crystalline phonon mode peak during the cooling stage of the experiment. Both the 165 and 230 cm^{-1} modes remain after the temperature ramp.

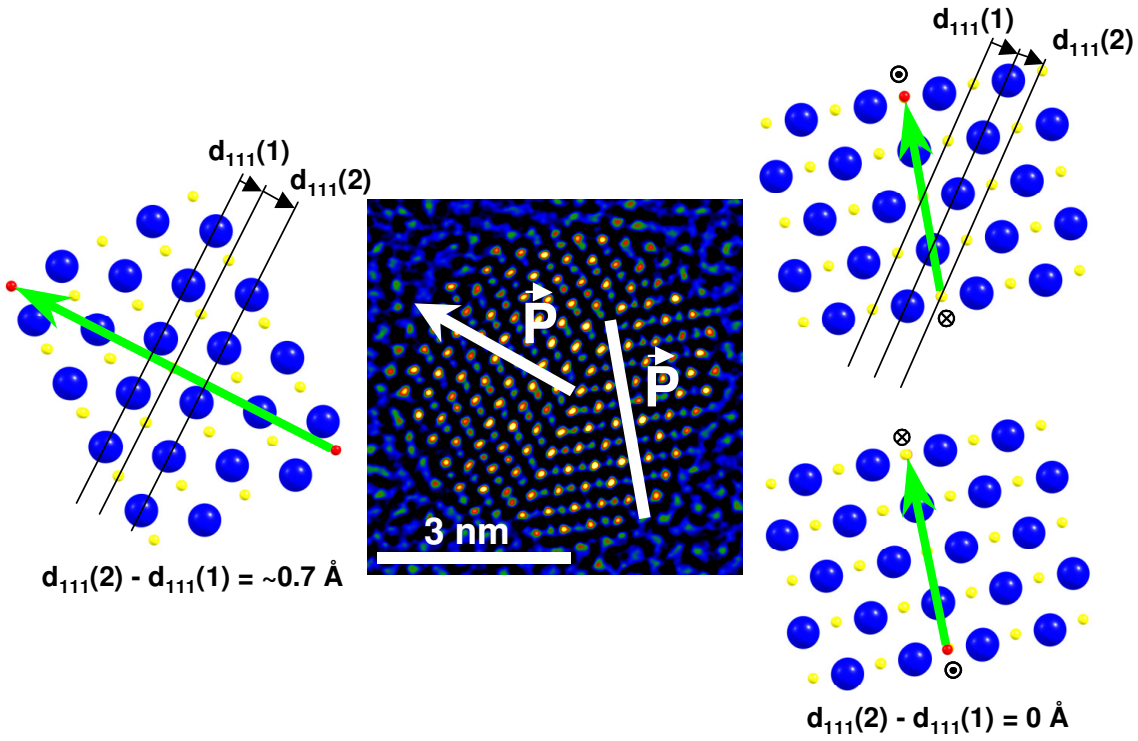

Fig. S4. Model of particle in Fig. 1d (main text). On the left side of the particle, the polarization direction can be fixed as shown using the direction of the sublattice displacement. On the right side of the particle, there are two possibilities for the polarization direction that cannot be definitively distinguished from the image alone. These possibilities can be determined from the absence of the {111} plane staggering and the slight upward displacement of the Ge sublattice (parallel to the in-plane component of the polarization vector). The two possible structures are distinguished by opposite directions of the out-of-plane component of the polarization vector. Structural parameters for the model are taken from reference 15 (main text).

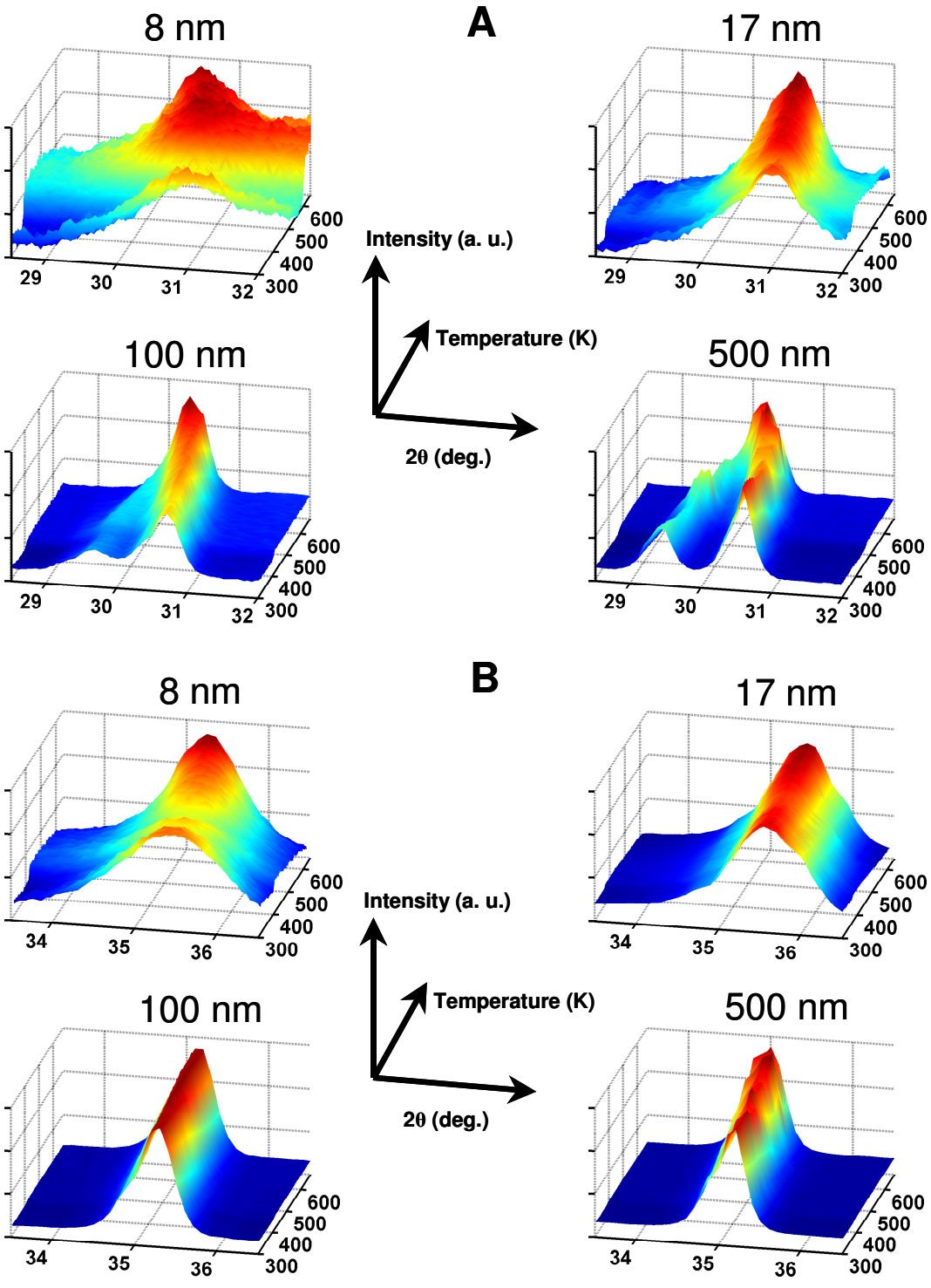
A
8 nm
17 nm
100 nm
500 nm
Intensity (a. u.)
Temperature (K)
2θ (deg.)
29
30
31
32
300
400
500
600
B
8 nm
17 nm
100 nm
500 nm
Intensity (a. u.)
Temperature (K)
2θ (deg.)
34
35
36
300
400
500
600

Fig. S5. Synchrotron x-ray diffraction data for GeTe nanocrystals. **(A)** Plots of diffracted intensity versus both 2-theta diffraction angle and temperature for the 003/021 doublet (derived from the cubic 111 diffraction line). **(B)** Plots of diffracted intensity versus both 2-theta diffraction angle and temperature for the 202 diffraction line (derived from the cubic 200 diffraction line), which remains a singlet throughout the transition.

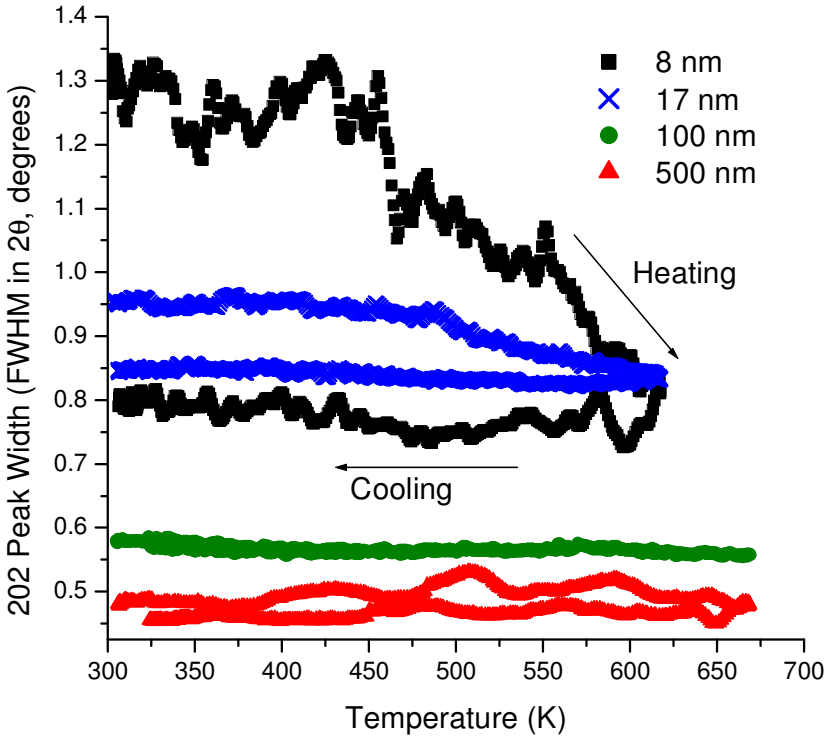

Fig. S6. Sintering analysis of GeTe nanocrystals. The full width at half maximum of the 202 (rhombohedral) peak, which remains a singlet over the entire temperature range studied, is plotted as a function of temperature for both the heating and cooling stages of the experiment. Negligible changes in the width of the peak are evident for the 100 and 500 nm nanocrystals. A coarsening of the 17 nm nanocrystals of less than 10 percent and a coarsening of the 8 nm nanocrystals of approximately 40 percent can be observed.

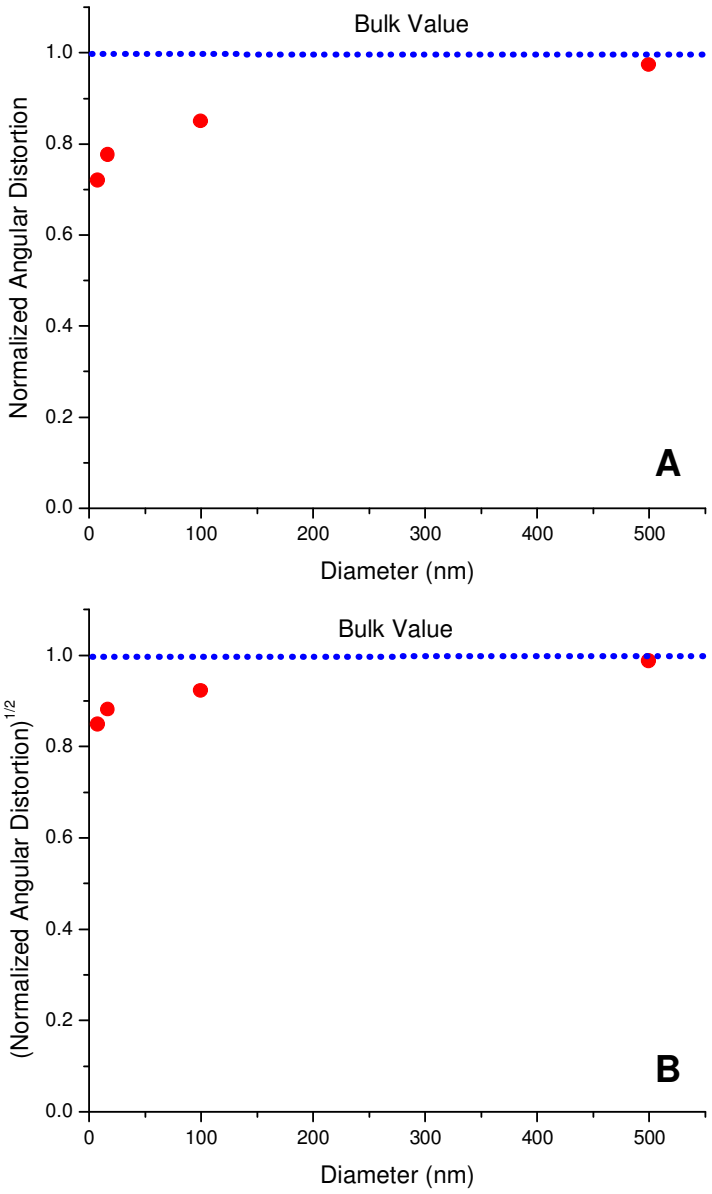

Fig. S7. Trends in angular distortion versus size determined by Rietveld refinement of synchrotron diffraction data. **(A)** Spontaneous angular distortion vs. average diameter for GeTe nanocrystals. The distortion is normalized to the bulk value taken from reference S6. **(B)** Square root of the angular distortion (normalized to bulk value), which is related to the spontaneous polarization, vs. particle diameter. Qualitative agreement with theoretical predictions of the scaling of the order parameter with size can be observed.